Available online at www.sciencedirect.com

SciVerse ScienceDirect

Journal of the European Ceramic Society 32 (2012) 2173–2185

www.elsevier.com/locate/jeurceramsoc

Fabrication and characterisation of cellular alumina articles produced via radiation curable dispersions

Judit Wilkens-Heinecke [a,b], Yoram de Hazan [a,*], Sascha Populoh [c], Christos G. Aneziris [b], Thomas Graule [a,b]

[a] *Laboratory for High Performance Ceramics, Empa, Swiss Federal Laboratories for Materials Science and Technology, Switzerland*
[b] *Institute of Ceramic, Glass and Construction Materials, TU Bergakademie Freiberg, Germany*
[c] *Laboratory for Solid State Chemistry and Catalysis, Empa, Swiss Federal Laboratories for Materials Science and Technology, Switzerland*

Received 22 August 2011; received in revised form 25 January 2012; accepted 12 February 2012
Available online 8 March 2012

Abstract

A general and versatile method for the production of cellular materials from radiation curable solvent-free colloidal ceramic dispersions containing pore formers has been developed. By this technique cellular ceramic articles with a precisely controlled porosity, cell size and shape are obtained for compositions containing solid pore formers. Monolithic bulk samples are obtained by thermal curing, whereas thin films and multi-layered articles are advantageously produced by UV curing. In this work the influence of three different spherical pore former types, PE, PS and PMMA, on the processing and final properties of the porous materials using alumina as model material is studied. The effect of pore former type and concentration on rheology, curing behaviour, debinding and sintering steps as well as thermal conductivity and mechanical strength of the sintered cellular materials is presented. It is also shown that the choice of pore former type modifies the sintering behaviour and resulting properties.

Keywords: Al_2O_3; Photopolymerisation; Porosity; Thermal conductivity; Mechanical properties

1. Introduction

Cellular ceramics are used in a broad range of engineering applications such as filters for molten metals or particles in gas streams,[1–3] in catalysis and separation,[4] as load-bearing lightweight structures or for thermal and acoustic insulation applications.[3] Most of these applications have rather strict requirements in terms of the morphology, e.g. cell size, cell window size and interconnectivity between the cells, and total porosity. These can be achieved by selection of an appropriate fabrication method. A wide range of fabrication methods were developed in the past.[1,5,6] Three different major approaches can be differentiated: ceramic foams produced by the replication of a sacrificial foam template,[7] direct foaming of a liquid slurry[6,8] or burn-out of fugitive pore former.[9–12] A wide range of fugitive pore formers are available and have been investigated, such as starch,[9–12] wax,[13] polymer beads,[14] saw dust and carbon.[15] In this paper the production of alumina (Al_2O_3) foams by the burn-out of polymeric beads will be presented. Given a suitable ceramic feedstock, the pore size and shape replicated in the final cellular ceramic can be controlled by the characteristics of the pore forming agents.

It is found that such cellular articles can be obtained with a feedstock consisting of a solvent-free, high loaded (with simultaneously low viscosity), radiation curable alumina dispersion containing solid polymer beads.[16] Curing of these compositions can be performed by thermal or UV–vis radiation. Alumina is in this paper used as a model material to demonstrate the process, but also other porous materials like hematite, titania and hydroxyapatite can be produced by this technique.[16,17] Likewise the polymer beads used in this study are used as a model material to demonstrate the good reproduction of size and shape of the pore formers. Depending on the final application, different pore formers with a wide variety of shape and size could be also used. Shaping the compositions by UV curing offers

Abbreviations: PF, pore former; PE, polyethylene; PS, polystyrene; PMMA, poly(methyl methacrylate); RT, room temperature; NPC, nominal pore former content; TSL, total solid loading.

* Corresponding author. Tel.: +41 0 433059168; fax: +41 0 433059168.
E-mail addresses: judit_heinecke@gmx.de (J. Wilkens-Heinecke), ydehazan@gmail.com, ydehazan@bluewin.ch (Y. de Hazan).

0955-2219/$ – see front matter © 2012 Elsevier Ltd. All rights reserved.
doi:10.1016/j.jeurceramsoc.2012.02.014

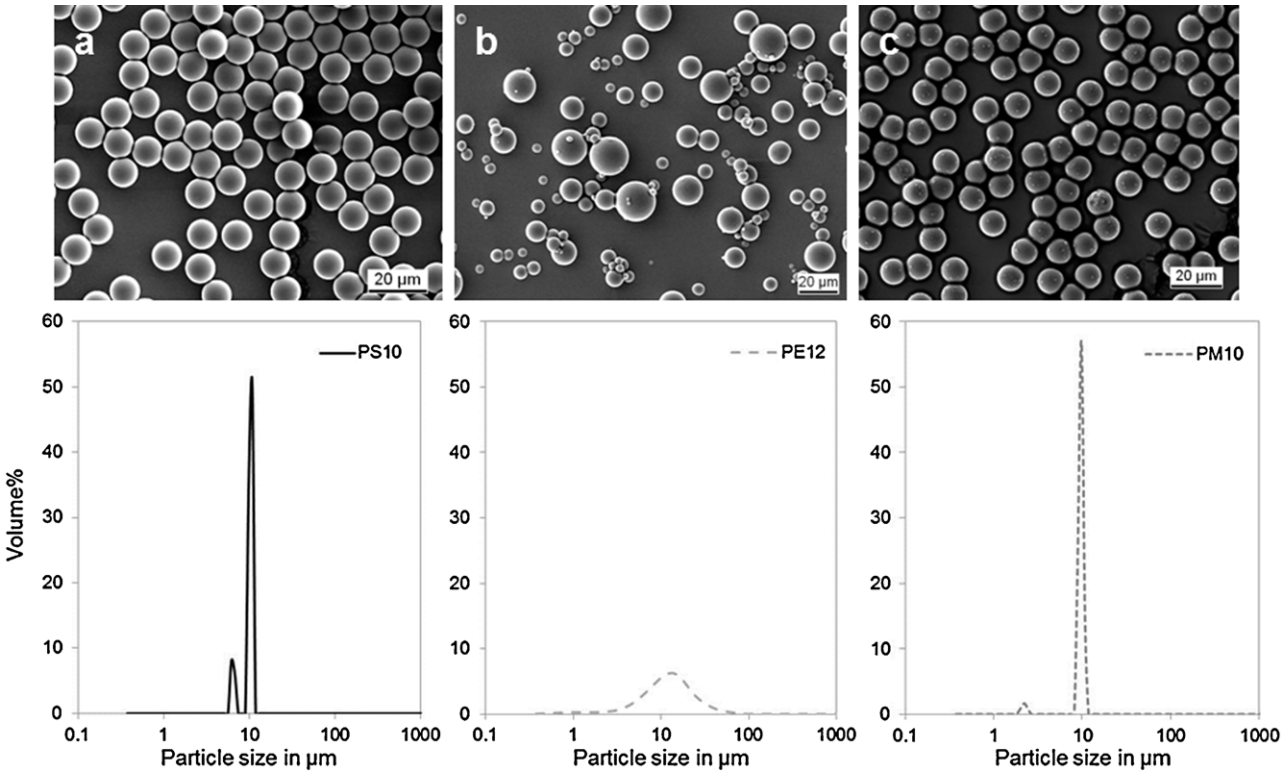

Fig. 1. SEM images and measurement of particle size distribution of pore formers used in this work: PS10 (a), PE12 (b), PM10 (c).

the possibility to lithographically pattern the pastes, similar to rapid prototyping/manufacturing.[18] By this near net-shape solidification method, which relies on solvent free dispersions and solid pore formers, complex cured samples can be obtained without stresses, due to low overall shrinkage.[18,19] Another advantage offered by UV curing of such pastes is the fast multi-layer shaping process, where in several minutes a shaped, solidified article is obtained at ambient conditions. Since no diluent is used, the interface between two cured layers is of high quality, which minimises defects, cracks and delamination. Nevertheless, shrinkage or deformation can still occur during the debinding process, therefore crosslinking of the matrix is necessary for shape retention during debinding.

The presented technique allows the production of cellular materials in a variety of shapes and with well-controlled cell morphology. In this paper the effect of different pore former types and concentration on the paste properties, shaping, the debinding and sintering processes is presented. The influence of pore formers on the resulting cell morphology, microstructure as well as mechanical and thermal properties is discussed.

2. Experimental

2.1. Materials

In this study TM-DAR (short TM), α-Al_2O_3 obtained from Taimei Chemicals Co., Ltd., Japan, was used. This powder has a mean particle size of 150 nm (according to measurements of particle size distribution by static laser light scattering with LS230, Beckman Coulter), a density of 3.98 g/cm^3 and a specific surface area of 12.5 m^2/g, measured by BET method with SA3100 (Beckman Coulter, USA). The alumina particles were sterically stabilised with MelPers4343 (MP), a commercial comb-shaped surfactant obtained from BASF, Germany.[20] This surfactant has a low charge density polycarboxylate backbone, polyether side-chain of 500 g/mole and a molecular weight of 20,000 g/mole. 4.5 wt.% per weight of alumina particle was used in this study for the stabilisation.

As UV curable media a mixture of 4-hydroxybutylacrylate (4-HBA; purity > 94%; from BASF, Germany) and poly(ethylene glycol) 200 diacrylate (PEG200DA; from Rahn, Switzerland) was used. This monomer mixture was used without any solvents or diluents and was mixed in the ratio 14:1 (4-HBA: PEG200DA). Chemical structures of the used monomers and also the photoinitiator LTM were already reported by Wozniak et al.[21]

Three different types of spherical polymer microbeads were used as pore forming agents (short PF), presented in Fig. 1. From Sumitomo Seika Chemicals Co., Ltd., Japan FLO-BEADS CL-2080 were obtained. These are polyethylene beads with a mean particle size of 12 µm (short PE12), a density of 0.92 g/cm^3 and a refractive index of 1.51. The second type of pore former were poly(methyl methacrylate) (Spheromers CA10) beads from Microbeads AS, Norway with a mean size of 10 µm (short PM10), density of 1.2 g/cm^3 and refractive index of 1.489 (non-cross-linked PMMA). PMMA beads are cross-linked and can contain up to 3% crosslinking agent which may increase its index of refraction. Polystyrene (PS) beads from Microbeads AS, Norway were the third type of used pore formers. They have a mean size of 10 µm and 40 µm (short PS10 respectively

PS40), a density of 1.05 g/cm^3 and a refractive index of 1.58. PS40 was obtained as commercial powder, however PS10 beads were obtained in a production solution and were separated by centrifugation, washed with water and dried at 60 °C for 24 h in order to be usable.

In Fig. 1 SEM images and particle size measurements of pore former in water with LS230 (Beckman Coulter, USA) present the characteristics i.e. form and size distribution of the three different pore formers used in this work. PMMA and PS spheres show a narrow, nearly monodisperse size distribution with a mean diameter of 10 μm. In contrast to this, the PE pore formers have a broad distribution, ranging from 1 up to 25 μm, with a mean diameter of 12 μm.

For the curing of the compositions by photopolymerisation the photoinitiator Genocure LTM, a liquid initiator blend consisting of ≤25% TPO (2,4,6-trimethylbenzoylphenylphosphineoxide, also known as MAPO – monoacylphosphine oxide) from Rahn, Switzerland was used. The initiator has an absorption range of 253–368 nm. An amount of 5 wt.% per monomer was used in all cases, which was added to the compositions shortly before curing.

For experiments with thermally initiated polymerisation, 2,2-azobis(2-methylpropionitrile) (AIBN, 98%; from Sigma Aldrich, USA) was used. 1% per monomer amount was added to the composition.

2.2. Paste preparation and characterisation

Powder with adsorbed MP4343 was produced as described by de Hazan et al.[20] by stabilisation in aqueous media and subsequent centrifugation, separation and drying of residue. 40 vol.% alumina dispersions were prepared by redispersing the obtained alumina powder with adsorbed surfactant in the 14:1 4-HBA-PEG200DA monomer mixture in a planetary ball mill (PM400, Retsch Inc., Germany). This milling was carried out with 3 mm ZrO_2 milling balls and a programme consisting of 40 min at 250 rpm, 15 min at 300 rpm and 15 min at 350 rpm, followed by short ultrasonication of the dispersion. Dispersions with lower solid loading than 40 vol.% were obtained by dilution with the monomer mixture.

In the following the term "dispersion" refers to the alumina slurry without pore formers and "paste" means the dispersion containing pore formers. If not otherwise mentioned the pastes were produced with 40 vol.% alumina dispersion. Pastes for the production of cellular materials were prepared by addition and mixing of the pore former into the dispersion. For the calculation of amount of pore former in the pastes the nominal pore former content (abbr. NPC) is used, which is similar to the nominal starch content defined by Gregorová and Pabst.[12] With this value the range of porosity of the resulting ceramics after firing can be estimated. It was calculated by the following equation: $NPC = V_{PF}/(V_{PF} + V_S)$, where V_{PF} represents the volume of the pore formers and V_S the volume of the alumina particles. For calculation of NPC no shrinkage of pores is taken into account, which means that NPC is not the same like real porosity of the sintered articles, instead the final porosity will be lower than this calculated value. An alternating description for the composition of pastes is the total solid loading (TSL). In this case the amount of pore former and alumina particles per paste will be given in the following as amount of $TSL = (V_{PF} + V_S)/V_{tot}$, where V_{tot} represents the total volume of the paste, e.g. resulting from the theoretical calculation 68.7 vol.% TSL corresponds to 70% NPC of the final sintered sample.

Rheological characterisation was performed with a rotational rheometer (Rheolab MC 120, Physica Messtechnik GmbH, Germany) as a function of shear rate in a concentric cylinder measurement device with a gap of 0.59 mm for pastes with different amount of pore formers. Measurements were carried out at temperatures of 10, 23, 30 and 40 °C. Before each measurement a temperature stabilisation of 30 min was conducted. The following measurement cycle, which was repeated three times, consisted of shearing at a constant rate of 10 s^{-1} for 3 min, followed by 22 measurement points from 10 to 1000 s^{-1} with logarithmic progression.

UV curing experiments, e.g. measurements of curing depths of the pastes respectively dispersions, were performed in a UV cube 100 equipped with a 100 W iron bulb (Dr. Hönle UV Technology, Germany). This UV source provides a 120 mW/cm^2 (significantly broadband) radiation spectrum in the UVA range, with a main peak at 360 nm and significant transmission around 405 and 440 nm.[21] Measurement of cure depths were performed by exposing the pastes to UV light for 15, 30, 60 and 120 s. To ensure curing of the composition from only one side, the mould was wrapped in aluminium foil for shielding from UV light. Cured films were washed and dried before measurement of thickness.

2.3. Shaping procedure, debinding and sintering

UV curable pastes and dispersions were cast in plastic moulds (16 mm in diameter and 1.5 mm thickness) and exposed to UV light, with 2 min from both sides. Thermally cured samples were cast in PTFE moulds (10 mm diameter, 20 mm height) and cured in an oven at 90 °C for 30 min. The density of cured samples was determined with the Archimedes method in water.

Cylindrical samples for the measurement of compression strength were prepared in a mould by multi-layering and UV curing or by thermal curing. For multi-layering, layers of ca. 200 μm thickness were cast and cured on top of each other till a thickness of ca. 1.5 cm was reached.

Debinding and sintering of cured samples was carried out in a chamber furnace from Carbolite RHF (Carbolite, UK). The programme consisted of a heating step with 0.9 °C/min up to 650 °C and a soak of 2 h for debinding, followed by a ramp of 1.5 °C/min up to 1500 °C and dwell time of 2 h for sintering and cooling back to room temperature (RT) with 1.5 °C/min.

2.4. Material characterisation

Cured samples were characterised by thermogravimetric analysis (TGA) and dilatometry, both analyses performed in air. TGA (TGA/DTA 851, Mettler-Toledo, Switzerland) of the cured green bodies and pore former were performed to

characterise the thermal decomposition. The heating profile consists of a 5 °C/min ramp up to 100 °C, followed by a hold of 30 min to remove weakly adsorbed water, followed by a heating ramp of 5 °C/min up to 850 °C. The debinding behaviour was analysed in the dilatometer DIL 802 (Bähr-Thermoanalyse GmbH, Germany). Dilatometry measurements of cured samples, having dimensions of approx. 12 × 5 × 1.5 mm, with and without pore formers were performed with a 2 °C/min ramp up to 650 °C, followed by 2 h dwell time and cooling to room temperature at 5 °C/min. Unlike other Dilatometry analyses, where the sintering process is observed, here only the debinding process is investigated to get an impression of the different burn out behaviour and hence different decomposition and influence of pore formers on cured samples. X-ray fluorescence (XRF) analysis was performed with PW 2400 (PANalytical, Netherlands) on the burn-out residue of PE pore formers. For this analysis Rhodium was used as anode element, a voltage of 60 kV and a current of 40 mA were applied and LiF(200), TlAP and PET crystals were used.

The microstructure of the cellular material was characterised by SEM and mercury intrusion porosimetry (MIP). Furthermore, mechanical properties were characterised by compression tests and thermal properties by analysis of thermal conductivity.

Mercury intrusion was carried out with Pascal 140/440 (Porotec GmbH, Germany) for determination of apparent and bulk density, as well as closed porosity and pore size distribution. The samples were intruded to a maximum pressure of 250 MPa. Spherical pores, resulting in a bottle-neck behaviour were chosen as the model. For analysis the Washburn equation was used, therefore a contact angle of 140° and a surface tension of 0.48 N/m were taken as a basis, resulting in a pore radius of 5.9 nm corresponding to the maximum pressure. The microstructure was characterised by scanning electron microscopy (VEGA Plus 5136 MM, Tescan instruments, Czech republic). Average grain sizes were estimated from SEM pictures of fracture surfaces of samples by applying a linear intercept method, here the number of grains is counted along line segments of known distance and the average value is calculated. Pore sizes were estimated by image analysis of fracture surfaces of pore structures. Therefore circles with known radii were fitted to the pores, the average pore size was calculated from ca. 65 fitted circles per sample.

Samples for compression tests and measurement of thermal conductivity were ground and polished with SiC paper grit size of P180 to obtain plane-parallel surfaces.

Compression tests were performed with a Zwick Z005 (Zwick GmbH & Co. KG, Germany) with a pre-load of 0.2 N and a test speed of 0.7 mm/min. For every investigated composition at least 4 samples were measured, the average values are reported.

Measurements of thermal conductivity were performed with Laser Flash method, carried out with LFA 457 MicroFlash (Netzsch, Germany). Tested samples had a diameter of 12.7 mm and a thickness between 0.9 to 1.2 mm. The measurement was carried out in argon from 50 to 1000 °C, the samples were coated with graphite before the measurement.

3. Results and discussion

3.1. Characterisation of curable pastes

3.1.1. Rheology

For the study and production of pastes containing PF dispersions containing 40 vol.% TM are used (unless noted). These dispersions show shear thinning behaviour with a viscosity of 265 mPas at 23 °C and shear rate of 500 s^{-1} (presented in Fig. 2a). According to particle size measurements conducted in water the dispersion is well stabilised with a mean particle size of 160 nm.

After addition of the pore formers to the dispersion, rheological measurements for different PF content in the pastes are performed to get an impression of the suitability of the different pastes for various shaping processes. In the following the rheological behaviour will be presented for pastes containing PE12, PS10, PS40 as well as the 40 vol.% dispersion without PF. Since the behaviour of PM pastes is influenced by other parameters, a small discussion about PM10 follows at the end of this section. All dispersions containing pore formers show shear thinning behaviour, which is shown exemplarily for dispersions containing PS10 and PE12 with 68.7 vol.% TSL (70% NPC) in Fig. 2a. These two PF were chosen to show the different influence of monodisperse (PS) and polydisperse (PE) systems on the rheology. As a comparison the 40 vol.% dispersion is also presented in Fig. 2. In comparison to the 40 vol.% dispersion, PF filled dispersions show a stronger shear thinning behaviour. PE12 shows the lowest viscosity over the whole measurement range of the PF filled systems, PS has a clearly higher viscosity. For high concentrations of PS10 (here 68.7 vol.% TSL), instabilities of the viscosity curve can be observed. This instability can be observed for a concentration of PS10 from 68.7 vol.% TSL onwards and occurs in the range of high shear rates. This unsteadiness of the viscosity curve can be a result of segregation/centrifugation effects,[22] which occur at higher shear rates (see Fig. 2a).

Fig. 2b presents the dependence of actual viscosity η (measured at 23 °C, 500 s^{-1}) on the inverse temperature (ranging from 10 to 40 °C) for compositions with 53.6 vol.% TSL (43% NPC) and 40 vol.% dispersion. As expected the dispersion without PF shows the lowest viscosity, PS10 composition has a lower viscosity than PE12, but the difference is only 0.03 Pas, which could be caused by measurement uncertainty. The decrease in viscosity with increasing temperature can be fitted to an Arrhenius function (presented by the dashed lines), which is described by Eq. (1) with A as a material constant (Pas), E_a the activation energy (J/mol), R the universal gas constant (8.314 J/K mol) and T the absolute temperature (K):

$$\eta = A \cdot \exp\left(\frac{E_a}{R \cdot T}\right) \quad (1)$$

Fitting with Arrhenius equation can be applied due to the linear relationship between the logarithm of viscosity and the inverse temperature. The Arrhenius equation is a widely used empirical equation for the description of the

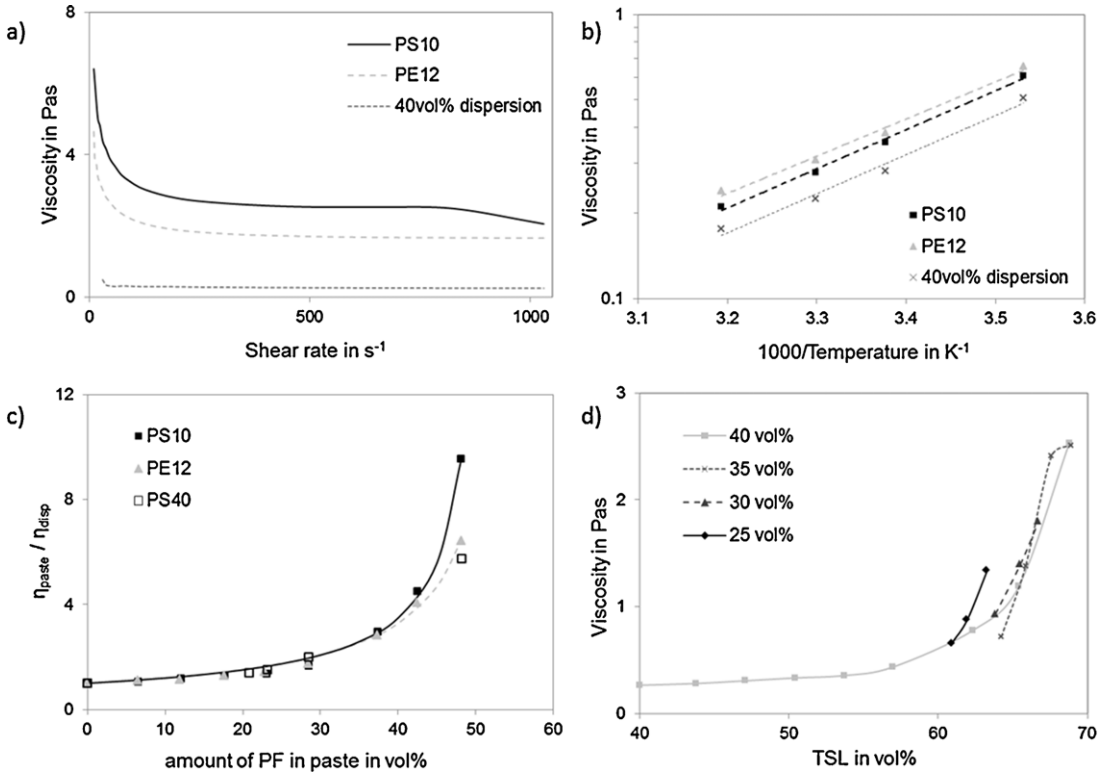

Fig. 2. Rheological measurements: (a) viscosity as a function of shear rate of pastes with 68.7 vol.% TSL (70% NPC) and 40 vol.% TM dispersion measured at 23 °C (b) viscosity of pastes with 53.6 vol.% TSL (43% NPC) and 40 vol.% TM dispersion as function of temperature^{-1} at 500 s^{-1} (c) relative viscosity of pastes as function of vol.% of different pore former in the paste at 23 °C and 500 s^{-1} (d) viscosity as function of TSL of pastes containing PS10 produced with different solid loading of TM dispersion at 500 s^{-1}.

temperature dependence of the viscosity.[23] The results of the fitting of the Arrhenius equation are presented in Table 1, showing good correlation coefficients in all cases. This indicates that the Arrhenius plot is suitable for the description of viscosity as function of temperature. All three compositions show a similar Arrhenius coefficient E_a/R, which is the slop of the fitted line, indicating similar temperature behaviour which is predominantly attributed to the monomer mixture and therefore PE and PS pore formers have no or only small influence. Also no significant difference between PE and PS can be seen, which leads to the conclusion that the size distribution of PF beads has no visible influence on the behaviour at the PF concentration studied here (53.6 vol.% TSL).

In Fig. 2c the effect of different amounts of pore formers on the viscosity is demonstrated for the PS10 and PE12 pore formers. Additionally also a slurry containing the bigger PS40 spheres is presented here. For the presentation of the rheological behaviour the viscosity of the pastes (η_{paste}) is normalised by the viscosity of the dispersion (η_{disp}) resulting in a relative viscosity $\eta_r = \eta_{paste}/\eta_{disp}$. Therefore, this relative viscosity displays the factor with which the viscosity of the dispersion is increased by the addition of pore former. This presentation is chosen to eliminate potential effects of the alumina dispersions on the results and therefore present clearly the effect of different pore formers on the viscosity as a function of pore former amount. As expected the viscosity increases with increasing amount of total solids and therefore also with increasing amount of pore former. This increase can be described by a modified Krieger–Dougherty equation,[24] given by Eq. (2) (φ_{eff} is the solid loading of pore former (in vol.%) in the paste, φ_{max} is the maximal theoretical solid loading of pore formers in the paste and n is a parameter for the description of increase in viscosity with increasing particle

Table 1
Parameters fitted to the Arrhenius equation (for 53.6 vol.% TSL pastes and 40 vol.% dispersion) and modified Krieger–Dougherty equations obtained for PS10 and PE12 pastes (at 500 s^{-1}).

Sample	Arrhenius parameters			Modified Krieger-Dougherty parameters			
	Constant A in $\times 10^{-5}$ Pas	Arrhenius exponent E_a/R in K	Correlation coefficient R^2	Maximal solid laoding φ_{max} in vol.%	Parametre n	Correlation coefficient R^2	Maximal NPC in %
PE12	2	3007.2	0.9913	56.02	0.95	0.9935	76.1
PS10	0.8	3160	0.9951	51.67	0.84	0.9956	72.8
Dispersion	0.7	3163.6	0.9847				

concentration). The Krieger–Dougherty equation is a well-known equation for the description of the viscosity function of concentrated suspension. However, in the modified version (Eq. (2)) the viscosity of a concentrated colloidal dispersion is used as the medium rather than the viscosity of a solvent.

$$\eta_r = \frac{\eta_{\text{paste}}}{\eta_{\text{disp}}} = \left(1 - \frac{\phi_{\text{eff}}}{\phi_{\max}}\right)^{-n} \quad (2)$$

It can be seen in Fig. 2c that the viscosity of the pastes show stronger dependency on the volume fraction in the case of the monodispersed PS10 compared to the polydispersed PE12 pore former, which is probably due to the difference in particle size distribution.[25] Due to this distribution the relative viscosity increases stronger from approx. 62 vol.% TSL onwards in case of PS10 compared to PE12. With a broader size distribution in case of PE12 smaller PE spheres can be packed in gaps between bigger spheres, resulting in an increase in maximal solid loading $\varphi_{\max}$, which results in a lower viscosity at the same solid loading for PE12 compared to PS10. The term $\varphi_{\max}$ is a critical solid loading concentration where the particles are packed at such high concentration that they block each other, and as result flowing of the dispersion is not possible anymore. Values for the critical concentration are presented in Table 1, along with the corresponding values for the nominal pore former content. From this figure also the influence of particle size is noticeable, here in case of PS10 and PS40. With decreasing pore former size the viscosity is clearly increased from 5.74 Pas to 9.55 Pas.

Fig. 2d presents a comparison of PS10 beads with TSL in the range of 40 up to 69 vol.% produced with TM dispersions having solids loading of 25–40 vol.%. The use of TSL results in this case in a conformity of the curves. The viscosity seems to be only a function of TSL not of the single components, neither alumina particles nor PS beads. An exception is the paste obtained with 25 vol.% dispersion. Here the effect of increasing PS fraction results in a stronger increase in viscosity. It is plausible that due to the relatively low TM content the paste segregates at higher PF volume fraction and therefore exhibits higher viscosities. This diagram shows that a higher TSL and therefore a higher porosity of the final samples, with suitable viscosity behaviour of the pastes can be achieved by increasing the pore former amount and proportionally decreasing the alumina amount.

PM10 pastes, similar to other dispersions containing PF also showed shear thinning behaviour, but instabilities of the viscosity curve, especially at TSL > 65.5 vol.% (65% NPC) occurring from ca. $100\,s^{-1}$ onwards, are observed. Further PM10 pastes always show the highest viscosities and somewhat different temperature behaviour (Arrhenius coefficient E_a/R of 2718 K). The unsteadiness of the viscosity curve could be a result of segregation/centrifugation effects or turbulences, similar to PS10 pastes. But due to the fact that the instabilities in case of PM10 occur over the whole shear rate range and also the higher overall viscosity, it is suspected that this behaviour is a result of a chemical interaction of PMMA spheres with the surrounding monomer matrix, perhaps attributed to a partial polymerisation of the monomer mixture around the PM10 particles caused by the cross linking agent in the PMMA itself. This would lead to higher viscosity because of partial solidification induced by slight thermal curing of the dispersion around the PMMA beads.

3.1.2. Photocuring

After rheological investigations the photoinitiator LTM, which contains TPO, is added to the pastes and the curing is performed. TPO features a high reactivity, resulting in high cure speed and strong absorption in the UV-A spectrum. Curing with LTM offers a good through-cure and is therefore suitable for the curing of thick pigmented layers.[26] The curing process of acrylate systems with initiation by TPO is explained by Decker et al.[27] To quantify the maximum thickness of cured samples, the cure depth of dispersions and pastes containing PF as a function of time is investigated. Knowledge of the cure depth and obtaining a homogeneous curing is also important for the production of multi-layered samples to prevent the enclosure of uncured pastes between cured layers, which could result in deformation, cracking and delamination during debinding and sintering. The cure depth depends on many variables such as temperature, light intensity, monomer reactivity, photoinitiator concentration and filler content and type.[28,29] An equation to describe the cure depth D_C depending on the energy dose E_0 in turbid ceramic suspensions was developed by Griffith and Halloran[30] and is given by Eq. (3), where d is the average particle size, $\Delta n = (n_p - n_0)$ refractive index difference between ceramic and medium, Q is scattering efficiency, E_{crit} is the critical energy dose required for photopolymerisation.

$$D_C = \frac{2d}{3Q}\frac{n_0^2}{\Delta n^2}\ln\left(\frac{E_0}{E_{\text{crit}}}\right) \quad (3)$$

Fig. 3 presents the cure depth of pastes and dispersion as a function of the energy dose, which is calculated from the curing time multiplied by the intensity ($120\,mW/cm^2$). In Fig. 3a a comparison of a 40 vol.% dispersion and pastes containing the three different pore former, each with 68.7 vol.% TSL (40 vol.% alumina dispersion with 70% NPC), is presented. In all curing curves the same progression is observable: a steep slope in the beginning caused by high amount of initiator radicals, followed by a flattening of the slope due to the consumption of available radicals and the decrease of the energy with increasing penetration depth. Polymerisation of the monomer matrix and scattering effects due to alumina particles limit the increase of the cure depth. The dispersion without PF shows the lowest cure depth and pastes with PE12 pore former the highest depth at all curing times investigated. For example at a curing time of 1 min (corresponding to an energy dose of $7200\,mJ/cm^2$) film thicknesses of 680 μm (PE12), 580 μm (PS10) and 480 μm (PM10) are measured for the pastes in comparison to 440 μm for 40 vol.% alumina dispersion.

The curing behaviour of the 40 vol.% dispersion without PF can be adequately described by Eq. (3), giving a critical energy dose of $363.8\,mJ/cm^2$ ($R^2 = 0.996$). However, Eq. (3) does not fully describe the PF filled systems (dashed lines, resulting R^2 of the fitting are 0.92–0.97). For all PF filled systems a similar trend can be observed: at low energy doses Eq. (3) seems to agree with measured values, but at higher energy doses the measured

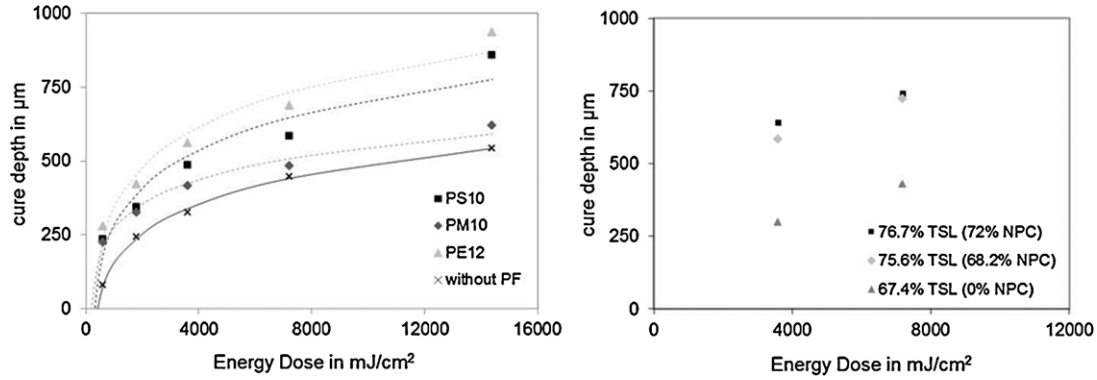

Fig. 3. Effect of energy dose E_0 on cure depth of 40 vol.% TM dispersion and pastes with 68.7 vol.% TSL containing different PF (left) and of pastes (made from 35 vol.% TM dispersion) containing different amount of PE12 (right).

values are higher than those predicted by Eq. (3). This observed deviation stems from the fact that the theoretical description (Eq. (3)), which is developed for 2-phase systems, gives incomplete description for the 3-phase systems studied here. In the paste there is scattering from three interfaces with different refractive index contrast (Δn): alumina–monomer, pore former–monomer and pore former–alumina. Nevertheless, it is seen that the PF filled systems exhibit higher cure depths. This probably stems from the fact that the refractive index of all the PF used here (1.49–1.58) is between that of the monomer (1.45) and the alumina particles (1.77). Low refractive index contrast implies better transparency for the UV light and therefore deeper penetration which results in higher cure depth.[30,31] PM shows the lowest cure depth of the filled systems, but due to the uncertainty in its refraction index it would not be appropriate to relate the trend in cure depth seen in Fig. 3a directly to the PF refraction index. Further, due to the three interfaces, the cure depth dependency of Δn and the volume fraction of the pastes may be complex.

In Fig. 3b the influence of the PE12 amount in the dispersion on the curing thickness can be seen. With increasing amount of PE12 the cure depth also increases. This observation agrees with the previous results that the use of PF increases the cure depth of pastes.

Densities of the cured samples are determined by the Archimedes method. The resulting densities of cured pastes (from 25% up to 70% NPC) and dispersions agree with the theoretical densities calculated by the rule of mixtures (Eq. (4)).

$$\rho_{\text{paste}} = \rho_{\text{PF}} \cdot v_{\text{PF}} + \rho_{\text{TM}} \cdot v_{\text{TM}} + \rho_{\text{monomer}} \cdot v_{\text{monomer}} \quad (4)$$

Cured 40 vol.% dispersion has a density of 2.32 g/cm^3 (compared to a theoretical density of 2.23 g/cm^3), thus showing a difference of 4%, indicating a small shrinkage during curing. The cured pastes show a similar trend. Here deviations (respectively maximal shrinkage) at low NPC of 25% of 4% (PE12), 3.5% (PS10) and 2.9% (PM10) are measured. Interestingly the shrinkage values decrease with increasing amount of pore former. For example in the case of PE12 the deviation between theoretical and calculated densities decreases from 4% (at 25% NPC) to 2.1% (at 70% NPC). These observations indicate that the differences between measured and theoretical densities are a result of the shrinkage of the monomer mixture[32] during curing and therefore the deviation decreases with increasing amount of pore former in the pastes.

3.2. Thermal debinding

In the following section the weight and dimensional changes occurring during thermal debinding are compared and discussed.

In Fig. 4 the TGA curves of cured samples with and without PF (left) and pure PF (right) are displayed in a temperature range from 100 to 700 °C. The PF amount in all experiments is 70% NPC (68.7 vol.% TSL). At 100 °C PS10 pore former shows a weight loss of 1.2% (Fig. 4, right), whereas PE12 and PM10 pore formers show ≤0.1% weight loss. This weight loss of PS10 seems to be related to water or other residue from the production solution (in which PS10 pore former were obtained). TGA curves of cured samples with and without PF show a similar progression: (I). a region before the polymer burn out starts from RT to 260 °C with a weight loss of not more than 2.5% for all tested samples. Such weight loss may be attributed to moisture, left over photoinitiator and/or a small fraction of unreacted monomer, (II) the main burn out region from 260 °C to approx. 420 °C showing a steep decrease where the main decomposition of the cured polymer and PF takes place (in case of PE12 this region is extended to 480 °C) and (III) a secondary burn out region up to 560 °C where residual carbon from II is removed. From here on no further weight loss can be seen. The cured polymer is completely burned out at a temperature of 560 °C leaving a remaining amount 71.5 wt.% alumina which is in good agreement with the 40 vol.% according to the composition. Pore formers are burned out completely (Fig. 4, right): PS10 at 430 °C, PM10 at 400 °C and PE12 at just below 550 °C. PM10 and PS10 beads burn out completely, but in the case of PE12 an unburned, likely inorganic residue of approx. 0.4 wt.% remains at 700 °C (see close up in Fig. 4). The curves of cured pastes show a qualitative overlay of PF and cured dispersion burn-out curves, which means that the turning points present in the curves of pure PF and dispersion are also present in the burn out curves of the pastes. The degradation of cured samples containing PS10 and PE12 are shifted to higher temperatures compared to PM10, which is also consistent with the degradation behaviour of the

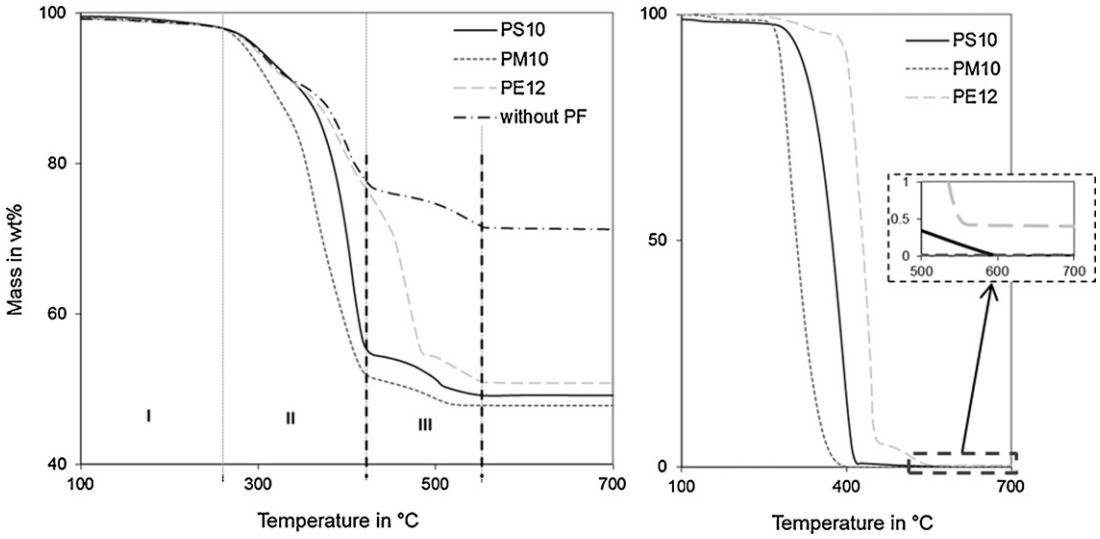

Fig. 4. TG analysis of cured samples produced from 40 vol.% TM dispersion and pastes with 68.7 vol.% TSL (70% NPC) containing different pore former (left) and pure pore former (right).

pure pore formers. This can be seen clearly for example in the burn-out behaviour of the cured PE composition. Here the primary burn out (region II) is stretched to 480 °C caused by the burn out behaviour of PE pore former. However, the PMMA beads seem to have an influence on the burn out behaviour of the cured matrix. While the first burn out step of the matrix (indicated by the left dashed line) is completed at 420 °C, for all PF systems, the second burn out step is completed for the PM10 system at a significantly lower temperature of 510 °C compared to 550 °C observed for the three other systems.

Dilatometry measurements were performed to assess the shrinkage involved in the debinding step up to 650 °C. The results for cured samples with and without PF are presented in Fig. 5. Similar to the TGA results (Fig. 4) the dilatometry curves also show three regions of shrinkage which corresponds to similar temperature ranges. During the first step (RT–260 °C), where little weight loss is observed by TGA, an expansion of the matrix is observed. The main shrinkage occurs in conjunction with the main burn-out step between 260 °C and 420 °C, but samples show significant shrinkage also during the second burn-out from 420–560 °C. The shrinkage in the PMMA system ends at a lower temperature compared to the other PF systems, which is in agreement with the TGA data discussed above. It is interesting to observe the influence of the three pore formers in the first step which involves no or little debinding. These can be influenced by the melting temperatures of the PF and a thermal expansion mismatch of the PF and the cured polymer matrix. Heating of the cured 40 vol.% alumina/polyacrylate composite results in an expansion of 0.9% up to 240 °C (Fig. 5), thus this is likely caused by the thermal expansion of the polymer matrix. Also samples with PF exhibit qualitatively an expansion up to 260 °C. Here the PE12 sample shows a much higher expansion, the maximal relative elongation is 3.4% (at 260 °C), compared to PM10 (0.9%) and PS10 (1.3%) samples. These observations are in qualitative agreement with the thermal expansion coefficient of the three different pore formers, which is the highest for PE12 with $1.7 \times 10^{-4}\,K^{-1}$ and lowest for PM10 with $5 \times 10^{-5}\,K^{-1}$, in the case of PM10 the crosslinking of PMMA beads can also have an effect on the good matching of the expansion of cured polyacrylate samples with and without PM10.

The final linear shrinkage at 650 °C of the PE sample is smaller than for the other two samples with PF. After a holding

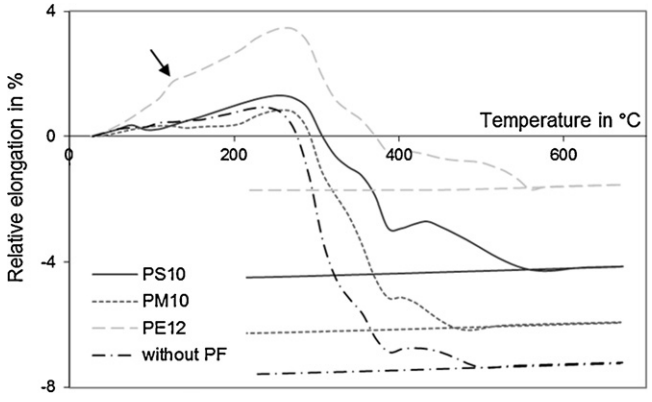

Fig. 5. Dilatometry analysis for the debinding process of cured samples of 40 vol.% TM dispersion and 68.7 vol.% TSL pastes containing different PF.

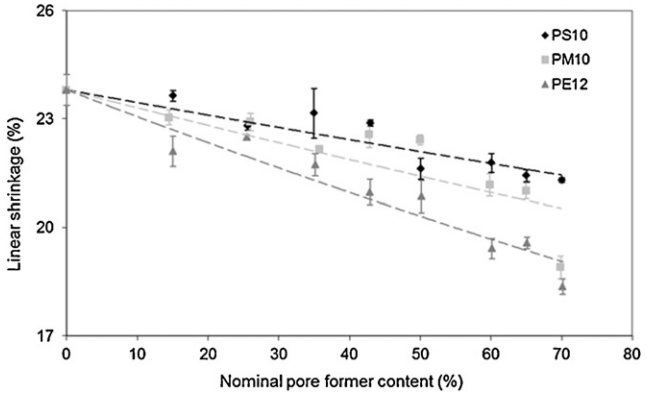

Fig. 6. Cumulative linear shrinkage of cured samples with different pore former types after sintering at 1500 °C as function of nominal pore former content.

time of 2 h at 650 °C the PE12 sample has shrunk by 1.6% compared to 6% for PM10 and 4.2% for PS10. The pore former free 40 vol.% alumina/polyacrylate composite shows highest shrinkage of 7.2%. The arrow in Fig. 5 marks a small hump in the PE curve at 110 °C, which corresponds to the melting temperature of PE. Even though the pore former may melt at this temperature the sample, and thus the polymerised monomer matrix appears to withstand the resulting expansion and maintains the macroscopic structure. The lower final shrinkage of PE12 sample may however be related to the relatively high expansion of the material during step I. It is possible that the alumina particles are pushed away from each other during the first step and this modifies their subsequent shrinkage during the other two steps.

Another observation in the dilatometry curves are humps for all curves around 400 °C. These humps are believed to be caused by the dilatometer itself, maybe as a result of a rapid burn out behaviour (see also Fig. 4 as reference).

Debinded samples of PM10, PS10 and PE12 show pore sizes of $9.4 \pm 0.2\,\mu m$, $9.5 \pm 0.3\,\mu m$ and $11.5 \pm 3.6\,\mu m$, determined by analysis of SEM images. These values correspond roughly to the measured shrinkage during dilatometry analysis.

3.3. Characterisation of sintered cellular material

3.3.1. Macro- and Microstructure

Fig. 6 presents the total linear shrinkage of cured bodies with TSL ranging from 40 to 68.7 vol.% (0% up to 70% NPC) after debinding and sintering for 2 h at 1500 °C. The measured standard deviation is relatively high (0.3–3% of mean value), yet it can be seen that linear shrinkage for all three pastes decreases with increasing TSL (or increasing porosity). For the 40 vol.% alumina/polyacrylate composite a shrinkage of 23.8% is measured, which corresponds roughly to the theoretical maximal shrinkage of 24.1% calculated for a cured sample with a measured density of $2.32\,g/cm^3$ (density of the cured bodies of 40 vol.% alumina/polyacrylate composite according to Archimedes method). Fig. 6 shows also that the linear shrinkage depends on the type of PF materials. PE and PS show the lowest and highest shrinkage at all NPC investigated, respectively and show linear dependency on NPC. The lower shrinkage observed for the PE may be attributed to the differences seen in dilatometry during the debinding step (Fig. 5). The trend for PM is not as predictable as the other two PF, perhaps due to thermal curing effects discussed in Section 3.1. Nevertheless, most linear shrinkage results fall between those of PE and PS. For the case most studied here of 70% NPC, PE12 and PM10 show a linear shrinkage of approx. 18–19%, whereas PS10 has 21.3%. This difference may indicate somewhat different sintering behaviour in the case of PS10.

In Fig. 7 the SEM images of typical microstructures observed at the fracture surfaces of sintered samples with a nominal pore former content of 70% are presented. It can be seen in Fig. 7 that the spherical shape of the pore formers is well reproduced in the sintered samples with all pore formers.[16,17] This fact can be attributed to the cross linked polymer matrix which could maintain the pore structure during burn out process. Also the characteristics of PF size distribution (see Fig. 1), meaning monodisperse distribution of PM 10 and PS and the broad distribution of PE 12 are well reproduced in the sintered materials (Fig. 8). The graph in Fig. 8 presents the pore size as a function of number-%. For PM10 and PS10 samples narrow pore distributions with pore diameters of $8.3 \pm 0.3\,\mu m$ and $8 \pm 0.2\,\mu m$, respectively are observed. This reduction in pore size compared to the initial PF size is due to the shrinkage of the samples during debinding and sintering. Calculated linear shrinkage of the pores of 17.1% for PM10 and 20.2% for PS10 is slightly smaller than the measured linear shrinkage of the whole sample of 18.9% and 21.3% (see Fig. 6). In the case of PE12 also a good reproduction of the PF distribution can be observed, the resulting pore size is in this case $9.7 \pm 4.6\,\mu m$. Also in the case of PE12 an approximate relationship between sample shrinkage and pore shrinkage can be observed. With a mean PF size of $12\,\mu m$ a linear pore shrinkage of 19.3% is calculated and thus corresponds also to the results from Fig. 6. In Fig. 7 a difference in the resulting microstructure of PE12 samples on the one hand and PS10 and PM10 samples on the other hand can be also observed. Whereas, the resulting grain size for PE12 samples is around 210 nm (indicating very little grain growth of the primary 150 nm TM-DAR particles), the grains of PM10 and PS10 samples average 600 nm and 665 nm and exhibit also a much broader distribution (300–1500 nm for PM10). The grain size of PM10 and PS10 samples is similar to the grain size of a sample produced from 40 vol.% dispersion without PF, here grains of approx. 620 nm are observed (Fig. 7d). In Fig. 7 the PE12 samples show mesopores, indicating the sample is not fully sintered, whereas the PS10 and PM10 samples appear fully sintered. These mesopores can be seen also in Fig. 9 and are discussed later. The difference in the grain size and sintering degree may be the result of the different expansion seen during the burn out of the pastes observed by dilatometry (Fig. 5). This means that the expansion of PE12 during debinding pushes the TM particles apart, reducing the contact between them, and would therefore result in a lower grain growth and degree of sintering. Another (or additional) explanation for the smaller grains can be an impurity in the PE12 beads. TGA results indicate the existence of this impurity because an unburned residue remains (see Fig. 4) after heat treatment up to 700 °C. XRF analysis of the inorganic leftover showed a composition of mainly Si, low fractions of Zn and Ca and traces of P, Al, Mg, Cu, Fe, Ti and K. It is assumed that those components are present in the form of an oxide. The traces are assumed to be caused partially by handling of the burned out pore formers and are negligible. The introduction of SiO_2 in an alumina system can result in smaller grains,[33] but it is worthwhile to note that such a composition in the pore formers should just influence a small area around the pores, but instead the complete sample shows small grains. An explanation could be the interplay of expansion and impurity, but this is beyond the scope of this work.

In Fig. 7 also cell wall thicknesses in the submicron range can be observed for all three PF types (down to 400 nm in the case of PS10). The cell windows connecting the pores estimated

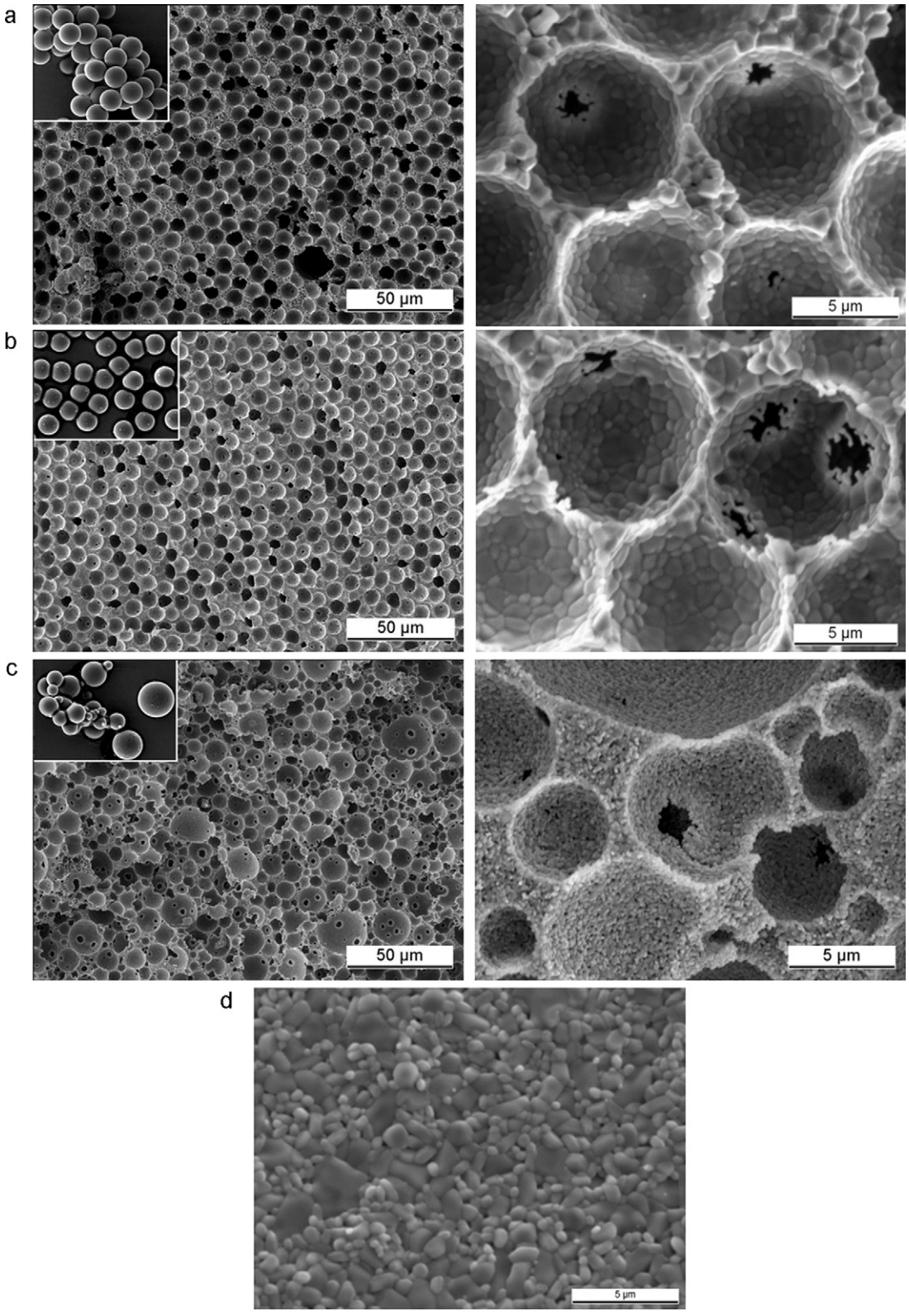

Fig. 7. SEM images of fracture surfaces of samples (40 vol.% TM, 70% NPC) sintered at 1500 °C produced with PS10 (a), PM10 (b) and PE12 (c) and sintered sample with 40 vol.% TM without PF (d). The inserts show the corresponding PF.

from Fig. 7 are in the range of 1–2 μm for all three samples. Such cell windows are a result of the direct contact between PF or a contact of PF with a very thin layer of alumina dispersion in between.

A more quantitative analysis of pore size and porosity of the samples shown in Fig. 7 (70% NPC) is done with MIP and presented in Table 2 and Fig. 9. Measured densities (bulk and apparent) and also open and closed porosity obtained by

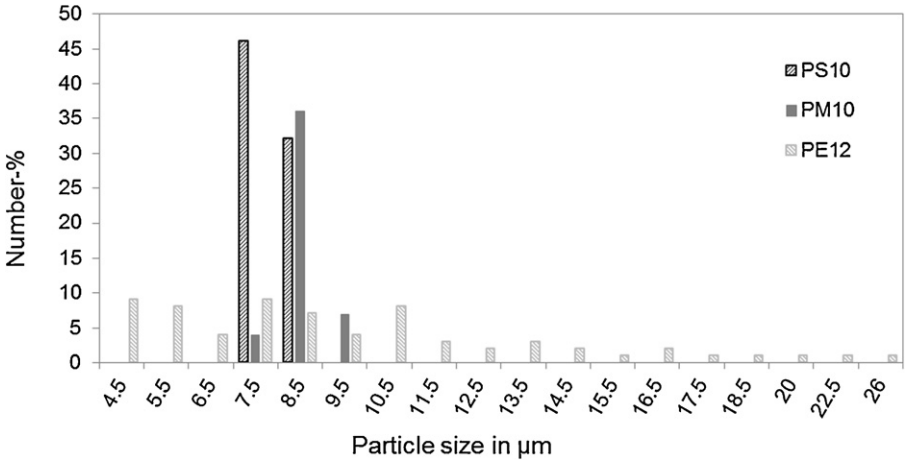

Fig. 8. Pore size distribution of sintered samples produced with PS10, PM10 and PE12 (70% NPC).

Table 2
Results of MIP measurements for samples with a nominal pore former content of 70%.

Sample	Average pore radius in µm	Bulk density in g/cm^3	Apparent density in g/cm^3	Open porosity in %	Closed porosity in %	Total porosity in %
70% NPC PE12	0.639	1.393	3.74	58.98	6.03	65.01
70% NPC PS10	0.874	1.605	3.73	53.39	6.28	59.67
70% NPC PM10	0.825	1.390	3.59	55.27	9.8	65.07

analysis of the sintered samples with MIP are presented in Table 2. Total porosity is calculated from the ratio of measured bulk density to the theoretical density of alumina of 3.98 g/cm^3. As expected this calculated porosity for all three PF types is lower than the nominal pore former content of 70%. Porosity of samples produced with PM10 and PE12 differ from the nominal pore former content by approx. 5%, the use of PS10 leads to a larger deviation (>10%) from NPC values. It is not clear at the moment why the use of PS10 shows a larger deviation, but this result is in agreement with the higher cumulative shrinkage (Fig. 6) and smaller pores observed during sintering.

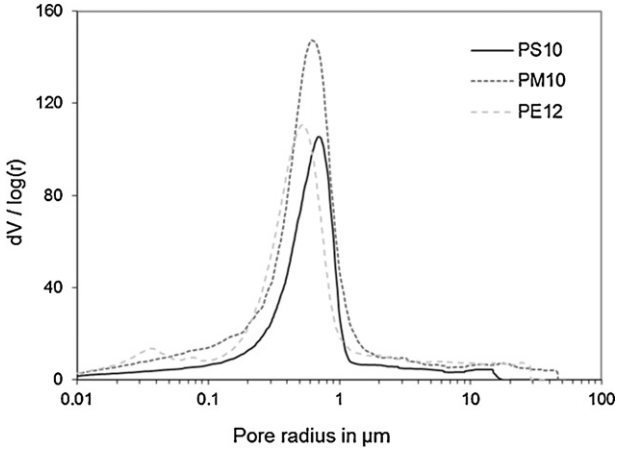

Fig. 9. Pore size distribution of sintered samples with 70% NPC produced with different pore forming agents measured by mercury intrusion porosimetry.

Average pore radii are measured to around 850 nm (Fig. 9), which is in agreement with the values predicted from cell windows seen in SEM (Fig. 7). If the measurement principle of MIP is taken into account and bottle-neck behaviour (which is also confirmed by the measurement) is assumed, the measured pores would be the smallest macropores. In this case the smallest macropores are the connection between pores, meaning the cell windows. For PE12 samples a small additional peak in the pore distribution can be seen in the range of 10–100 nm, which is attributed to the observed mesopores (Fig. 7).

In Fig. 10 additional examples for cellular materials are presented in the SEM images to demonstrate the possibility to produce for example articles with larger pore size (Fig. 10a) or higher porosity (Fig. 10b and c). Fig. 10a demonstrates that larger PF (PS 140 µm) are well replicated in the cellular material after sintering yielding a pore diameter of ca. 115 µm (which corresponds to ca. 21% linear shrinkage, at 70% NPC). Again cell windows can be observed, but with a size of ca. 8 µm, which is caused by larger contact areas between larger pore formers having smaller radius of curvature. This was also observed in other studies.[34]

As discussed in Section 3.1 cellular materials with higher porosities can be produced by the technique employed here. The cellular material in Fig. 10b is produced with a composition containing 25 vol.% alumina dispersion and a pore former amount corresponding to 80% NPC. The sample has a pore size of ca. 7–8 µm, with cell windows of 2–3 µm. The smaller pore size compared to the 70% NPC PS10 sample is a result of the higher shrinkage of the base dispersion. A 25 vol.% alumina/polyacrylate composite should exhibit a linear shrinkage of 37% compared to 24.1% for a 40 vol.% alumina/polyacrylate

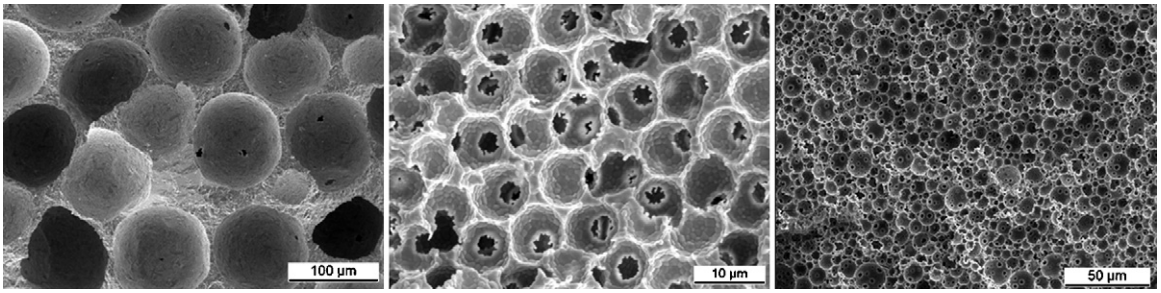

Fig. 10. Examples showing versatility of the shaping method: (a) cellular article produced with PS 140 µm and 70% NPC, (b) cellular article with 80% NPC produced with PS10 in 25 vol.% dispersion and (c) cellular article with 85% NPC produced with PE12 in 30 vol.% dispersion.

composite. Another example of materials with higher porosity is given in Fig. 10c. This sample is produced from a 30 vol.% dispersion filled with PE12 with 85% NPC. According to MIP analysis the resulting sintered sample has a total porosity of 79% and cell window size of 0.75 µm.

It is worthwhile to mention that even with big pore former size or high amount of pore former (and therefore diluted alumina dispersion) the pastes remain stable over the curing process and samples with homogenously distributed pore formers after curing are obtained.

3.3.2. Mechanical strength and thermal conductivity

To determine the suitability of the produced cellular materials for thermal insulation purposes the thermal conductivity and also compression strength are measured and listed in Table 3. Values of thermal conductivity (λ) are calculated from the thermal diffusivity a, specific capacity c_p and density ρ of the sample with the Eq. (5).

$$\lambda = a \cdot c_p \cdot \sigma \quad (5)$$

Thermal diffusivity a is obtained from the temperature increase as a function of time which results from the heating of the examined samples from one side. The specific heat capacity as a function of temperature is derived by measuring a standard sample (Pyroceram 9606) with known c_p under the same conditions as the examined samples, a similar procedure is performed also e.g. by Ahn et al.[35] At room temperature alumina has a thermal conductivity of ca. 30 W/m K.

Samples produced from PE12 show a lower thermal conductivity compared to the other samples. This difference can be partially attributed to the higher porosity of PE12 compared to PM10 and PS10, but since the differences in porosity are considered small, the main reason is the much smaller grain size of the samples. Therefore, PE samples exhibit more grain boundaries, which results in a higher thermal resistance per unit area[36] compared to PM10 and PS10 samples with much bigger grains. It is assumed that the polydispersity of PE samples is not the major reason for the difference in thermal conductivity. Even though PM10 and PS10 samples have the same porosity the thermal conductivity is slightly different. This could be caused by the different sinter behaviour already observed in SEM images.

It is also necessary to mention that the LFA method is not the most suitable analysis method for thermal conductivity of highly porous materials. Therefore, samples with porosity >60–70% are difficult to measure by LFA.

The compression strength of UV cured multilayer samples produced with the various PF show a large variation (Table 3). PE12 samples show a compression strength of 75 MPa, whereas PS10 and PM10 only 28.4–32.5 MPa. This difference could be attributed to the broader pore size distribution of PE samples and/or to the smaller grain size. According to Studart et al.[6] the compressive strength of alumina with a porosity of 60–70% averages 100–30 MPa for a closed or open cell morphology, respectively, Kamitani et al.[34] report values in a similar range of the PE samples (95 MPa for 58% porosity). The compression strength of the polydisperse PE samples produced by UV curing is comparable to these literature values, which are also reported for polydisperse systems. However, the monodisperse PS10 and PM10 UV cured sample show much lower values. This could also be attributed to the layer-by-layer production, which is necessary to produce larger UV cured samples. During the production, defects at the interfaces may occur which influence the compression test. These may also include accumulation of pore formers at one interface. Interfacial defects can be avoided when thermal curing is employed. The thermally cured PM10 sample shows here a much higher strength (at a comparable porosity) than the UV cured PM10 sample (Table 3).

Table 3
Compression strength thermal conductivity of samples obtained with different pore formers and curing strategies. Samples sintered at 1500 °C for 2 h.

	Compression test		Tests of thermal conductivity			
	Porosity in % (geometrical)	Compression strength in MPa	Porosity in % (geometrical)	λ at 100 °C in W/m K	λ at 500 °C in W/m K	λ at 900 °C in W/m K
70% NPC PE12, UV cured	62.8	75.1	63.4	2.2	1.3	1.4
70% NPC PS10, UV cured	62.4	28.4	60	5.7	2.6	2.2
70% NPC PM10, UV cured	63.9	32.5	60	6.5	2.9	2.7
70% NPC PM10, thermally cured	64.1	59.6				

4. Summary

In this paper the influence of pore former (PF) type, size and concentration on the processing of cellular materials from solvent free, radiation curable compositions were investigated. It has been demonstrated that cellular alumina articles having spherical pores ranging from 8 up to 140 μm, corresponding closely to the initial shape of the PF, and porosities up to 79% can be obtained by this technique.

Stable pastes of alumina dispersions loaded with pore formers showing shear-thinning behaviour can be produced. The viscosity shows an almost universal dependency on the total solid loading (TSL, including ceramic particles and PF) of the pastes. This implies that cellular materials of higher porosity can be processed similarly by increasing the ratio of PF to ceramic particles while keeping their total concentration in the paste constant. The curability of pastes by either thermal or UV irradiation is demonstrated. The presence of the pore formers investigated here significantly increases the cure depth of the composition compared to the dispersion without PF. The pore former type has a major effect on the resulting microstructure and final mechanical and thermal properties. The use of PE pore former results in cellular materials having small grains (210 nm) and mesopores, whereas the use of PM and PS pore former leads to fully sintered bodies with larger grains (>600 nm). The PE samples also exhibit higher compression strength (75 MPa compared to 28.4 MPa respectively 32.4 MPa) and lower thermal conductivity (1.4 W/m·K compared to 2.2 W/m K respectively 2.7 W/m K at 900 °C) than PS and PMMA samples. Also the curing strategy influences the mechanical properties. The use of thermal curing results in higher compression strength (59.6 MPa compared to 32.4 MPa).

Acknowledgement

The authors would like to thank Urs Gfeller from Department of Corrosion and Materials Integrity, Empa for performing XRF measurements.

References

1. Scheffler M, Colombo P. *Cellular ceramics*. Weinheim: Wiley-VCH; 2005.
2. Gauckler LJ, Waeber MM, Conti C, Jacob-Duliere M. Ceramic foam for molten-metal filtration. *J Metals* 1985;**37**:47–50.
3. Montanaro L, Jorand Y, Fantozzi G, Negro A. Ceramic foams by powder processing. *J Eur Ceram Soc* 1998;**1**:1339–50.
4. Coronas J, Santamaría J. Catalytic reactors based on porous ceramic membranes. *Catal Today* 1999;**51**:377–89.
5. Colombo P. Conventional and novel processing methods for cellular ceramics. *Phi Trans R Soc A* 2006;**364**:109–24.
6. Studart AR, Gonzenbach UT, Tervoort E, Gauckler LJ. Processing routes to macroscopic ceramcis: a review. *J Am Ceram Soc* 2006;**89**: 1771–89.
7. Schwartzwalder K, Somers AV. Method of making porous ceramics articles. US Patent 3 090 094; 1963.
8. Sepulveda P, Binner JPG. Processing of cellular ceramics by foaming and in situ polymerisation of organic monomers. *J Eur Ceram Soc* 1999;**19**:2059–66.
9. Gregorová E, Pabst W, Zivcová Z, Sedlárová I, Holíková S. Porous alumina ceramics prepared with wheat flour. *J Eur Ceram Soc* 2010;**30**:2871–80.
10. Bowden ME, Rippey MS. Porous ceramics formed using starch consolidation. *Key Eng Mater* 2002;**206**(213):1957–60.
11. Lyckfeldt O, Ferreira JMF. Processing of porous ceramics by 'starch consolidation'. *J Eur Ceram Soc* 1998;**18**:131–40.
12. Gregorová E, Pabst W. Process control and optimized preparation of porous alumina ceramics by starch consolidation casting. *J Eur Ceram Soc* 2011;**31**:2073–81.
13. da Silva MHP, Lemos AF, Gibson JR, Ferreira JMF, Santos JD. Porous glass reinforced hydroxyapatite materials produced with different organic additives. *J Non-Cryst Solids* 2002;**304**:286–92.
14. Luyten J, Mullens S, Cooymans J, De Wilde AM, Thijs I. New processing techniques of ceramic foams. *Adv Eng Mater* 2003;**5**:715–8.
15. Wang H, Sung IY, Li XD, Kim D. Fabrication of porous SiC ceramics with special morphologies by sacrificing template method. *J Porous Mater* 2004;**11**:265–71.
16. de Hazan Y, Graule T, Heinecke J. Shaped cellular articles and (micro)spheres. European patent 09005854, PCT/CH2010/000109; 2009.
17. de Hazan Y, Märkl V, Heinecke J, Aneziris C, Graule T. Functional ceramic and nanocomposite fibers, cellular articles and microspheres via radiation curable colloidal dispersions. *J Eur Ceram Soc* 2011;**31**:2601–11.
18. Halloran JW, Griffith M, Chu T. Stereolithography resin for rapid prototyping of ceramics and metals, US Patent 6117612; 2000.
19. Esposito Corcione C, Greco A, Montagna F, Licciulli A, Maffezzoli A. Silica moulds built by stereolithography. *J Mater Sci* 2005;**40**:4899–904.
20. de Hazan Y, Heinecke J, Weber A, Graule T. High solids loading ceramic colloidal dispersions in UV curable media via comb-polyelectrolyte surfactants. *J Colloid Interface Sci* 2009;**337**:66–74.
21. Wozniak M, Graule T, de Hazan Y, Kata D, Lis J. Highly loaded UV curable nanosilica dispersions for rapid prototyping applications. *J Eur Ceram Soc* 2009;**29**:2259–65.
22. Leighton D, Acrivos A. The shear-induced migration of particles in concentrated suspensions. *J Fluid Mech* 1987;**181**:415–39.
23. Zhou G, Willett JL, Carriere CJ. Temperature dependence of the viscosity of highly starch-filled poly(hydroxyl ester ether) biodegradeable composites. *Rheol Acta* 2000;**39**:601–6.
24. Bergström L. Rheological properties of concentrated, nonaqueous silicon nitride suspensions. *J Am Ceram Soc* 1996;**79**:3033–40.
25. Shapiro AP, Probstein RF. Random Packings and Fluidity Limits of Monodisperse and Bidisperse Suspensions. *Phys Rev Lett* 1992;**68**:1422–5.
26. Glöckner P, Jung T, Struck S, Studer K. *Radiation curing for coatings and printing inks: technical basics and applications*. Hannover: Vincentz Network; 2008.
27. Decker C, Zahouily K, Decker D, Nguyen T, Viet T. Performance analysis of acylphosphine oxides in photoinitiated polymerization. *Polymer* 2001;**42**:7551–60.
28. Lee JH, Prud'homme RK, Aksay IA. Cure depth in photopolymerization: experiments and theory. *J Mater Res* 2001;**16**:3536–44.
29. Tomeckova V, Halloran JW. Cure depth for photopolymerization of ceramic suspensions. *J Eur Ceram Soc* 2010;**30**:3023–33.
30. Griffith ML, Halloran JW. Scattering of ultraviolet radiation in turbid suspensions. *J Appl Phys* 1997;**81**:2538–46.
31. Chartier T, Hinczewski C, Corbel S. UV curable systems for tape casting. *J Eur Ceram Soc* 1999;**19**:67–74.
32. Jacobs PF. *Rapid prototyping and manufacturing fundamentals of stereolithography*. Dearborn, MI: Society of Manufacturing Engineers; 1992.
33. Kebbede A, Parai J, Carim AH. Anisotropic grain growth in α-Al_2O_3 with SiO_2 and TiO_2 additions. *J Am Ceram Soc* 2000;**83**:2845–51.
34. Kamitani K, Hyodo T, Shimizu Y, Egashira M. Fabrication of highly porous alumina-based ceramics with connected spaces by employing PMMA microspheres as a template. *Adv Mater Sci Eng* 2009;**2009**:1–9.
35. Ahn K, Li C, Uher C, Kanatzidis MG. Improvement in the thermoelectric figure of merit by La/Ag cosubstitution in PbTe. *Chem Mater* 2009;**21**:1361–7.
36. Poulier C, Smith DS, Absi J. Thermal conductivity of pressed powder compacts: tin oxide and alumina. *J Eur Ceram Soc* 2007;**27**:475–8.